Insights Into the 2020 Instability Crisis of Merapi Through Numerical Modeling

M. Galárraga, Luc Scholtes, B. Chevalier, Nurnaning Aisyah, Karim Kelfoun

Insights into the 2020 Instability Crisis of Merapi through Numerical Modeling

M. Galárraga[1], L. Scholtès[1], B. Chevalier[2], N. Aisyah[3], and K. Kelfoun[1]

[1]Université Clermont Auvergne, CNRS, IRD, OPGC, Laboratoire Magmas et Volcans, Clermont-Ferrand, France.
[2]Clermont-Auvergne INP, Institut Pascal, Université Clermont Auvergne, Clermont-Ferrand, France.
[3]Ministry of Energy and Mineral Resources, Geological Agency, Center for Volcanology and Geological Hazard Mitigation, Indonesia.
Corresponding author: Michael Galárraga (mikegalarraga@hotmail.com)

Key Points:

- Discrete element models are utilized to assess the stability of Merapi's flanks
- The inelastic deformation of Merapi's NW flank during the 2020 eruption was caused by magma pressurization and reached a stable state
- Our study suggests that a 500 m deep portion of Merapi's flank was mobilized during the crisis

Abstract

The northwestern flank of Merapi volcano (Java, Indonesia) moved from July 2020 to January 2021. The cliff collapses at the summit, the size of the affected area (about 500 m in elevation and 1 km wide) and a flank displacement of about 14 m, never observed before, led to fears of a flank collapse. Field observations suggested a correlation between this flank movement and the opening of a NE-SW fracture crossing the entire summit, filled with magma. In the present study, we developed numerical models based on the discrete element method to investigate the role of the NE-SW fracture pressurization on the deformation of Merapi. Even though simplified, considering the complexity of the processes at stake, our approach manages to reproduce the observed deformations both in terms of kinetics and kinematics. Specifically, the model reproduces the inelastic deformation of the northwestern flank to a depth of about 500 m below the summit. Under the pressure of the magma, the northwestern flank tilted slightly, causing its sliding with displacement magnitudes increasing with elevation. As observed on-site, the sliding eventually stopped so that the flank reached a new stable state, demonstrating how topographic readjustments of a volcano, driven by magma pressure, can produce significant plastic deformation without leading to a major flank collapse.

Plain Language Summary

Between July 2020 and January 2021, the northwestern flank of Merapi volcano in Java, Indonesia, experienced unusual movements. A large fracture, running from northeast to southwest across the summit and filled with magma, appeared to be linked to this movement. Using computer simulations, we tested how the pressurization of this fracture could have caused the observed deformation. Our results reproduce the pattern of the flank movement recorded on-site. The simulations indicate that magma pressure caused the northwestern flank to tilt slightly and slide outward. This sliding affected the flank to a depth of about 500 meters but eventually stopped without leading to a catastrophic collapse. These findings suggest that volcano flanks can undergo relatively large and permanent deformations as a result of magma pressure without necessarily failing, which is crucial for understanding volcanic hazards and improving monitoring strategies.

1. Introduction

Merapi volcano (Java, Indonesia) is known for its activity of dome growth, gravitational dome collapse, and for the associated pyroclastic currents (Gertisser et al., 2023). However, recent observations showed that its activity is far more complex than previously known, with multimetric deformations, sliding, and collapses affecting both the summit and its flanks (Global Volcanism Program, 2021; Grémion, 2024).

After the emplacement of the 2018-2019 lava dome (Kelfoun et al., 2021), a series of explosions opened a NE-SW fracture at the summit of Merapi. Satellite images (Bemelmans, 2025) show that the fracture length progressively increased and, subsequently, by July 2020, a large sector of the northwestern flank of the volcano began to move (Figure 1). At the summit, this movement led to major collapses affecting the crater walls, reaching 50 to 100 m in height and comprising several tens of millions of cubic meters of material (Figure 1c). Electronic distance measurements (EDM) on the northwestern flank (reflector RB1), made by the Merapi's Observatory (Global Volcanism Program, 2021), indicated a northwestward displacement of about 10 m over a period of 7 months, with a maximum rate of 17.5 cm/day (Figure 1b). These displacement magnitudes have since been confirmed by our stereoscopic calculations (VELI-BPPTKG data, up to 18 m at the summit) and by satellite imagery (Grémion, 2024) which also show that the displaced zone was 1 km wide (Figure 1a). In January 2021, after 7 months of deformation, the flank displacement ceased with the extrusion of two lava domes: one extruding from the tip of the fracture, on the SW flank, and the other one at the center of the summit crater (Figure 1a). The deformation resumed in July and decreased in August 2021 (Figure 1b), following a peak in the eruptive activity of the SW lava dome.

This 2020-2021 crisis raises several fundamental scientific questions. What were the primary factors driving the flank instability? Were these movements primarily controlled by local stress conditions, material strength, or magmatic pressures within the edifice? Most critically, was the deformation limited to the surface, or did it extend to deeper levels? Indeed, given that the crisis was primarily analyzed through surface deformation measurements, the possibility of a deeper and more complex failure surface cannot be ruled out. Thus, the collapse potential remains a major concern, particularly considering past large-scale flank failures, such as the 1980 Mount St. Helens debris avalanche (Criswell, 1987; Voight et al., 1983). Knowing whether such deformations are superficial or could lead to a debris avalanche is fundamental in terms of decision-making and human safety. It is therefore necessary to find a methodology that would be relevant to investigate such a case.

During the last decades, volcanic edifice instabilities have been studied through several methods, from the classic limit-equilibrium methods (LEM) (Donnadieu et al., 2001; Reid et al., 2000; Schaefer et al., 2013), through laboratory experiments or analogue models (Acocella, 2005; Cecchi et al., 2004; Tibaldi et al., 2006; van Wyk de Vries & Merle, 1998), to numerical modeling (Apuani et al., 2013; Bozzano et al., 2013; Heap et al., 2021; Russo et al., 1997). While LEM are simple to use and widely accepted, they come with several limitations. For instance, LEM formulation is purely plastic with no consideration of elastic deformation and progressive failure processes. The predefinition of the sliding surface geometry as well as the localization of the

mechanical analysis along the sliding surface are other limitations of LEM. Also, the basal stress state in LEM formulations is ultimately a function of gravitational loading on the individual slices. Thus, the influence of topographic and stiffness-based variations in the underground stress state cannot be considered (Diederichs et al., 2007). Alternatively, analogue models have proven to be valuable for understanding complex volcanic edifice deformation processes (Norini & Acocella, 2011). Nevertheless, they are often constrained by material properties, scale effects, and difficulty in replicating complex geological conditions (Kavanagh et al., 2017). Numerical modeling, on the other hand, allows for greater flexibility in incorporating heterogeneous material properties, complex geometries, as well as representative mechanical behaviors and boundary conditions. It also enables a more detailed analysis of stress distribution and failure mechanisms.

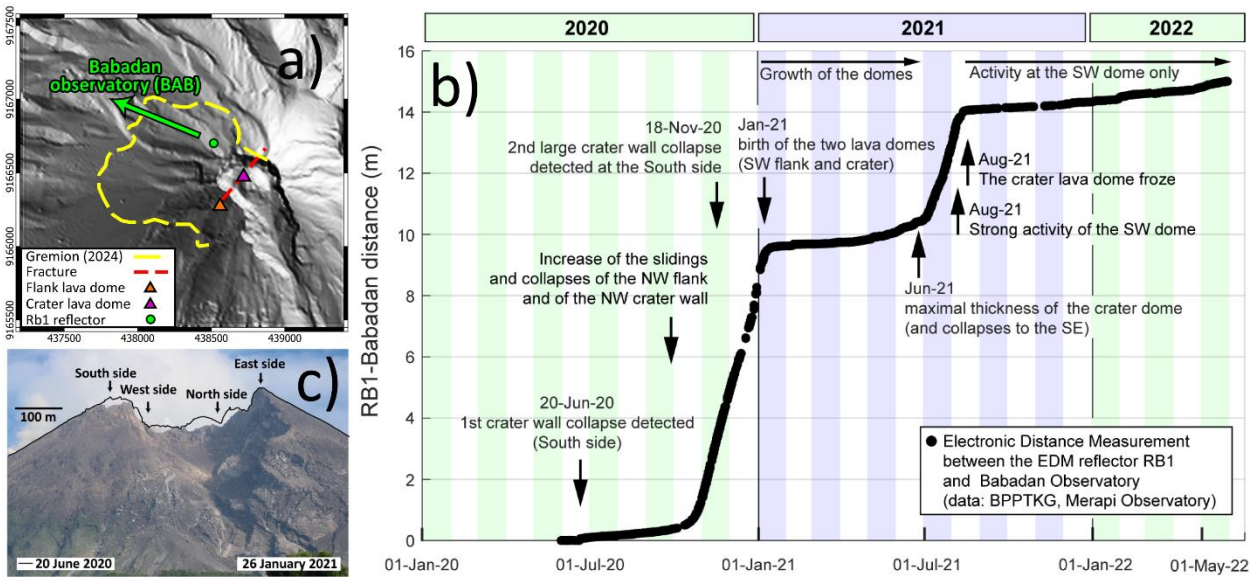

Figure 1. (**a**) Digital elevation model of Merapi volcano showing the zone that deformed during the 2020-2021 crisis (dashed yellow contour), according to Grémion (2024). The location of the NE-SW fracture, 2021 lava domes, Rb1 reflector, and the direction toward the Babadan (BAB) observatory are also depicted in the image. (**b**) Changes of slope distance Rb1-BAB during the period from 1 June 2020 to 31 May 2022 measured by the Merapi's Observatory (BPPTKG). (**c**) Southeast view from the Kalor station showing the crater in January 2021, with the black line indicating the shape of the summit in June 2020 (VELI-BPPTKG data).

In recent years, several numerical approaches have been successively utilized to study volcano flank deformation related to magmatic activity. For instance, Beauducel et al. (2000) presented three-dimensional elastic boundary elements method (BEM) models to study the 1993-1997 Merapi volcano deformation by taking into account topography, summit discontinuities and different types of deformation source including dome weight, magma pressure and shear stress within the conduit. Green et al. (2006) using BEM models, and Albino et al. (2011), Marsden et al. (2019) and Neuberg et al. (2018) using finite element method (FEM) models, explained surface tilt variations through shear stress variations along the conduit at the Soufriere Hills (Montserrat), Mount St. Helens (United States) and Tungurahua (Ecuador) volcanoes, respectively. However, these studies only considered the elastic behavior of the volcanic edifices, which is a limitation considering the cohesive-frictional nature of volcanic rock

materials. As such, elastoplasticity (Currenti et al., 2010) and viscoelasticity (Del Negro et al., 2009; Hickey et al., 2013; Le Mével et al., 2016) have been implemented in FEM models dedicated to the study of volcanic ground deformation. Nevertheless, the deformation processes modeled by these last studies were not related to upper conduit processes, but to overpressures related to relatively deep magma chambers, located at depths ranging from 4 to 17 km. Moreover, most of these numerical studies were based on 2D descriptions. However, although 2D models can provide useful insights into deformation mechanisms (e.g., Albino et al., 2011), they are limited when applied to real 3D objects. Indeed, as stated by Cayol and Cornet (1998), topographic features significantly influence volcanic deformation, making it essential to incorporate realistic topographies into such analyses (Apuani et al., 2013; Casagli et al., 2009).

In the present study, we propose to use 3D discrete element method (DEM) models to study the multimetric displacements observed at Merapi during the 2020-2021 crisis. Besides its capability to model complex nonlinear behaviors representative of different rock types (Scholtès & Donzé, 2013), the DEM enables to explicitly describe progressive failure mechanisms without any assumption on a predefined sliding surface, making it a powerful tool for slope stability analysis (e.g., Jensen & Moore, 2023; Mreyen et al., 2022; Scholtès & Donzé, 2012, 2015; Huber et al., 2024). Moreover, DEM models have recently proven to be successful in describing different volcanic processes (Harnett et al., 2018; Holohan et al., 2011; Morand et al., 2024).

In the following, we present a numerical analysis of the 2020-2021 Merapi crisis. Firstly, we describe the methodology we used to generate the synthetic Merapi volcano and the approach we implemented to simulate the magma pressurization within the NE-SW fracture. Secondly, we showcase our results, beginning with a parametric study dedicated to illustrating how mechanical properties control the volcano stability and its failure behavior. Then, based on the model's predictions, we explore the kinetics and kinematics of the 2020-2021 instability. Finally, and considering the assumptions made, we discuss the possible consequences for the future flank behavior of Merapi.

2. Method

2.1 DEM formulation

2.1.1 Particle model

DEM models discretize the medium into discrete elements (DEs; see Figure 2 for illustrations of the discretization) that interact with one another through contact forces (Cundall & Strack, 1979). These contact forces are computed based on the relative displacements occurring between each pair of DEs according to predefined behavior laws (also called "contact laws"). In the present study, we used the bonded particle model (BPM) proposed by Scholtès and Donzé (2013) for modeling rock materials and implemented in the YADE platform (Angelidakis et al., 2024; Smilauer et al., 2021). This BPM decomposes interparticle forces into normal and shear components, respectively noted F_n and F_s. In compression, the normal force F_n is given by the linear relation,

$$F_n = -k_n \Delta D;$$

where ΔD is the relative displacement between the interacting DEs, and k_n is the normal stiffness defined by:

$$k_n = E_{eq} \frac{R_A R_B}{R_A + R_B};$$

where E_{eq} is an equivalent bulk modulus and R_A and R_B are the respective radii of the interacting DEs (A and B).

In tension, F_n is computed with the same stiffness as in compression for small deformations. A maximum admissible tensile force $F_{n,max}$ is defined as a function of the local tensile strength t_p such that:

$$F_{n,max} = -t_p A_{int};$$

where $A_{int} = \pi(_{min}\,(R_A, R_B))^2$ is the interacting surface between each pair (A, B) of interacting DEs.

The shear force F_s is computed in an incremental way by updating its orientation and magnitude based on the shear force increment $\Delta F_s = k_s \Delta u_s$ which develops at the interaction point, as described by Luding (2008):

$$F_s = \{F_s\}_{updated} + k_s \Delta u_s;$$

with k_s and Δu_s being the shear stiffness and the relative incremental tangential displacement, respectively.

The maximum admissible shear force is defined through a Mohr-Coulomb criterion such as:

$$F_{s,max} = F_n \tan \varphi_p + c_p A_{int}$$

where φ_p is the local frictional angle and c_p is the local cohesion.

If either $F_s \geq F_{s,max}$ or $F_n \geq F_{n,max}$, shear or tensile rupture of the bond occurs, respectively, and a "crack" is assigned at the former bond location. From this point onward, the interaction is deleted or becomes purely frictional (i.e., t_p=0 and c_p=0) if the contact is maintained between the DEs (i.e., if shear rupture occurred under a compressive state). New contacts created during the simulation are also treated as purely frictional.

2.1.2 Numerical scheme

The numerical scheme of the DEM consists in several steps: (a) the interaction forces between each pair of DEs in contact are computed based on the contact law according to their relative position (see section 2.1.1), (b) the resultant forces on each DE are used to determine their respective acceleration following Newton's second law of motion, (c) the acceleration is then time integrated, using an explicit finite difference scheme, to find the new position of the DEs. This process is repeated iteratively over the entire simulation. In addition, to dissipate energy and favor the quasi-static response of the models, a local non viscous damping strategy is used (Duriez et al., 2016). It is designed to decrease the resultant force by an opposite force $(\Delta F)_d$ defined as:

$$\frac{(\Delta F)_d}{F} = -\lambda_d sgn(F\,\dot{u}^o)$$

where λ_d is the damping coefficient (fixed to 0.5 in our simulations) and $sgn(F\,\dot{u}^o)$ indicates the sign of the dot product between the net force F acting on the particle and the previous mid-step velocity $\dot{u}^o$.

2.2 Simulation setup

To investigate the 2020-2021 Merapi crisis, we considered the following observations: (a) a NE-SW fracture was detected on the summit (Bemelmans, 2025), slightly off-centered to the NW of the crater (Figure 1a), with a surface trace length of 450 m by October 2020, (b) the eruptions of two lava domes occurred on January 2021, at the SW tip of the NE-SW fracture and at its center, indicating that the fracture was filled with magma, and (c) the deformation slowed down right after the lava domes formed (Figure 1), suggesting that magma pressure was the driving mechanism of the deformation.

From these observations, we hypothesized that the instability was related to the rise of magma through the NE-SW fracture. Thus, we built 3D DEM models of Merapi volcano containing the NE-SW fracture (Figure 2) (see Text S1 for details of the numerical volcano generation). The volcano is treated as a homogeneous medium (see section 4.1 for a discussion of this assumption) without predefined sliding surface and with dimensions of 4,620 × 4,620 × 2,109 m. The NE-SW fracture is modeled as a discontinuity plane with a trace length of 450 m, extending vertically from the crater floor (z_{pt} = 2,805 m) down to the base of the model (z = 805 m), and positioned 70 m to the NW from the crater center, as suggested by the satellite images from Bemelmans (2025). In order to gain computational efficiency, the model, built from a digital elevation model with a horizontal resolution of 15 m, was packed with 267,673 DEs following an adaptive strategy: the DEs have a diameter equal to 25 ± 8 m on the 800 m upper part of the volcano, while their sizes increase linearly with depth up to 100 ± 32 m.

Gravity is applied in combination with roller boundary conditions (normal displacements are blocked) on the sides and at the bottom of the model to generate lithostatic stresses within the model corresponding to a material density ρ_{rock} of 2,500 kg/m^3 as proposed by Heap et al. (2021) in a numerical study dealing with a volcanic edifice presenting similar settings in terms of composition (i.e., andesitic) and eruptive dynamics (i.e., lava dome activity) (see also section 2.3 for a justification of the homogeneous medium assumption). The density of the DEs is defined as $\rho_p = \rho_{rock} * V / V_p$, where V is the volume of the model and V_p is the total particle volume (see Text S2 for details).

The effect of magma is modeled as a set of pressure forces applied along the NE-SW fracture walls (see Text S3 for details of the implementation). The pressure is magma-static along the lava column height, considering a density of 2,400 kg/m^3 as suggested by Beauducel et al. (2000). To take into account the 2021 crater lava dome that reached an elevation z_d of about 2,855 m by February 2021 (Grémion, 2024), we added an overpressure of 1.2 MPa that corresponds to the 50 m dome thickness.

To quantify the deformation, marker particles were located around the center of the summit, on the upper flanks (Figure 2a). In the northwest direction (the direction of the observed flank deformation), four marker particles (p1, p2, p3, p4) were located approximately 100 m under the volcano topographic surface to characterize the movements at depth (Figure 2c).

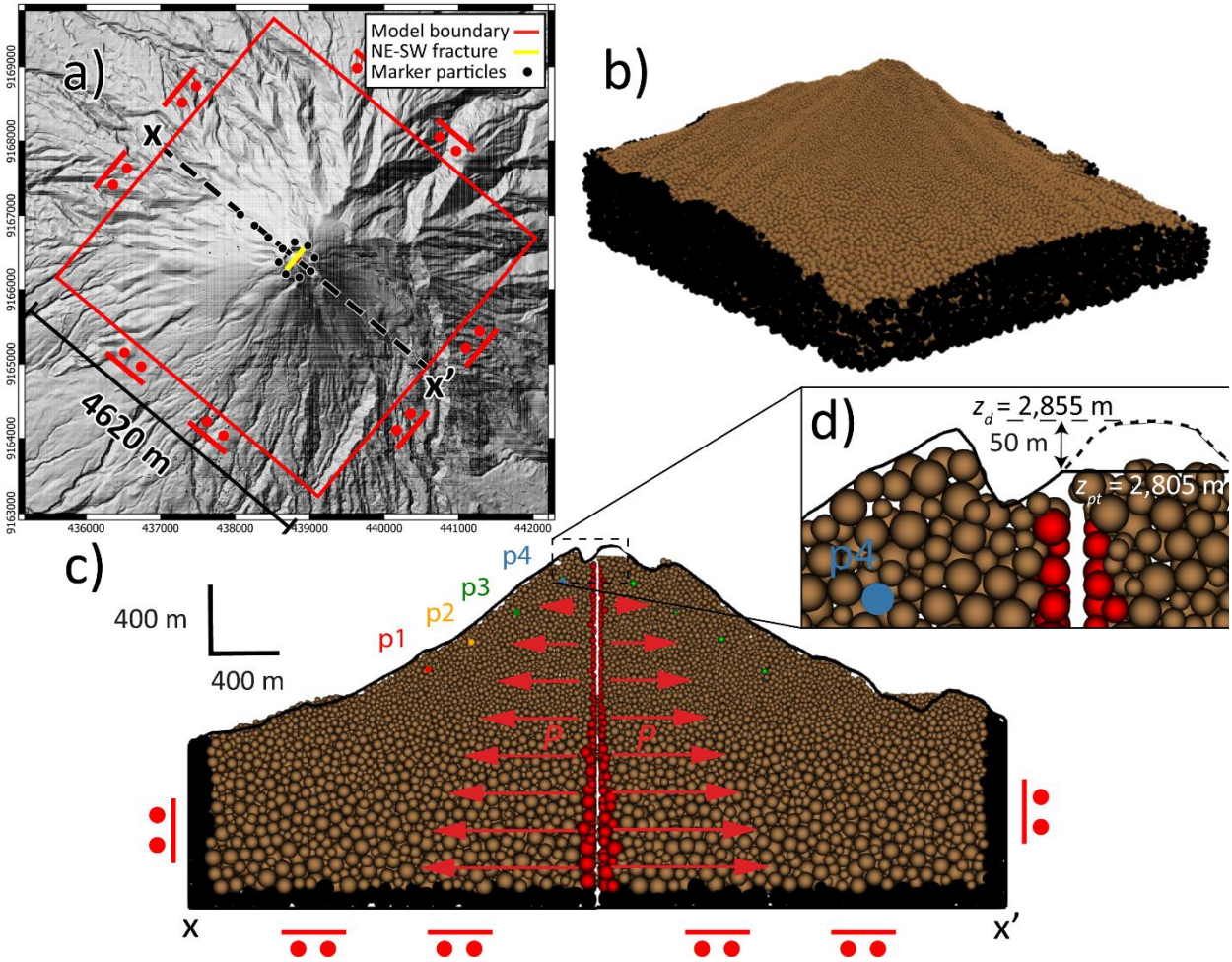

Figure 2. (**a**) Top view of Merapi digital elevation model showing the horizontal extent of the DEM model, the NE-SW fracture trace, the marker particles, and the lateral roller boundary conditions. The location of the x-x' cross section, which has a N130°E direction, is defined by the dashed black line. (**b**) DE assembly used to model Merapi: darker particles define the boundary conditions. (**c**) x-x' cross section showing details of the DE assembly as well as the bottom and lateral roller boundary conditions. The p1, p2, p3 and p4 marker particles are also shown. The red particles define the fracture walls. The red arrows represent the pressure forces applied to the fracture wall (perpendicularly to the fracture plane). The dashed black rectangle at the summit demarcates Figure 2d. (**d**) Inset displaying the height difference between the crater floor (2010 plateau top, z_{pt} = 2,805 m) and the 2021 crater dome summit (z_d = 2,855 m).

2.3 Mechanical properties

The structure and composition of Merapi volcano are complex and reflect its long eruptive history, which began before 170 ka ago (Gertisser et al., 2012). According to Gertisser et al. (2023), this history can be subdivided into three major evolutionary stages or temporal volcanic edifices: Proto-Merapi, Old Merapi and New Merapi. The oldest edifices (Proto-Merapi and Old Merapi) are composed mainly of basaltic–andesite lavas intercalated with pyroclastic deposits. The most recent cone (New Merapi) was constructed after major flank collapses and explosive events that produced a horseshoe-shaped structure opening toward the southeast (Figure. 1a).

The present summit consists of basaltic–andesitic lava domes, with older domes truncated and partly covered by younger ones, and interbedded pyroclastic rocks. Lithological and structural heterogeneities are thus present at all scales. Because it is not feasible to characterize the mechanical properties of each individual unit and to identify their respective spatial extension, we assume homogeneous material properties in this study. This simplifying assumption is discussed later in section 4.1.

In DEM (particle) models, global material behaviors (i.e., emergent mechanical properties of the particle assembly at the scale of the volcano) arise from DE interactions (i.e., local or interparticle properties which are the model input parameters) but cannot be directly inferred from them. Therefore, a procedure is necessary to relate the model's parameters to the emergent mechanical properties. It usually consists in performing a series of mechanical tests (Scholtès & Donzé, 2013) on subsamples of the model with a given set of interparticle properties to determine the emergent mechanical properties by analyzing the stress-strain curves resulting from the simulations. In the present study, because we performed a back analysis of the Merapi's flank instability, we systematically performed this procedure to identify the material properties from the model parameters (see Text S4 for an example of this procedure). In the following, the emergent properties (volcano scale) are noted c and ϕ for cohesion and friction angle respectively; while the interparticle properties (particle scale) are called c_p, t_p, and φ_p for cohesion, tensile strength, and friction angle, respectively.

3. Results

Here below, we present the main results of our study, beginning with the back analysis of the 2020-2021 instability crisis we used to determine the mechanical properties of Merapi volcano. Then, based on the results of this analysis, we propose a characterization of the 2020-2021 instability in terms of kinetics and kinematics.

3.1 Back analysis

3.1.1 Strength Reduction method

To determine the mechanical properties (i.e., c and ϕ) that led Merapi volcano to destabilize, we used a strength reduction (SR) method (Bonilla-Sierra et al., 2015; Matsui & San, 1992). First, the model is loaded into the simulation with high strength properties (i.e., c_p, t_p, and φ_p) and is let to settle under the combined effect of gravity and magma pressure (450 m column height associated to an overpressure of 1.2 MPa, see section 2.2). Then, the strength properties are progressively decreased until the model destabilizes (see Text S5 for details of the SR method we used). In this study, we considered that the volcano slopes were stable if the displacement magnitudes recorded by the marker particles (p1-4) were smaller than those measured in the field during the crisis (about 10 m as presented in Figure 1). Additionally, we considered that the volcano was stable if the velocities of the marker particles tended toward zero after deformation. At this point, one has to note that we had to define the elastic properties of our model to perform this stability analysis. We chose to set the elastic properties of the model based on an upscaling of the laboratory values presented by Harnett et al. (2022), so that our

synthetic volcano has a Young's modulus, *E*, equal to 8 GPa and a Poisson's ratio, ν, equal to 0.3. These values were obtained using the empirical scaling approaches proposed by Hoek and Diederichs (2006) and Vásárhelyi (2009), respectively, with a Geological Strength Index (GSI) of 55 as recommended by Heap et al. (2020) for a volcanic rock mass. We analyze the influence of these elastic properties on our results in section 3.2.3.

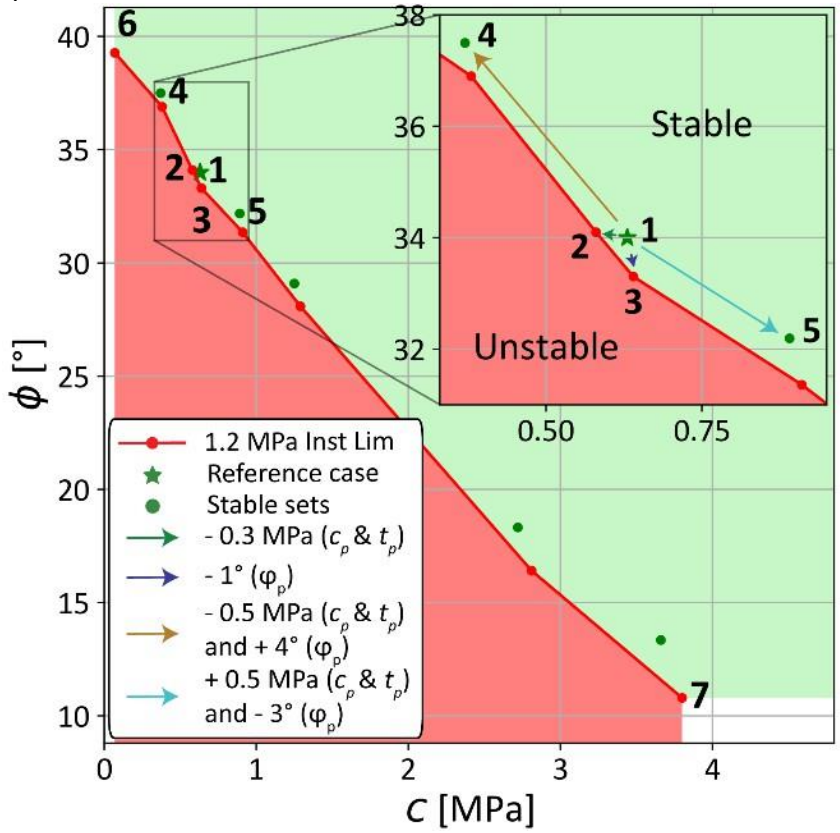

Figure 3. Stability analysis of Merapi volcano in the {*c*, ϕ} plane when subjected to magma pressurization (see section 2.2 for details). Green markers represent the stable cases (Sets 1, 4 and 5). Set 1, depicted with a star, is our reference case discussed in section 3.2. Red markers represent unstable cases (e.g., Sets 2, 3, 6 and 7) and, thus, define the instability limit. The corresponding model parameters and emergent mechanical properties are given in Table 1. Green, blue, brown and sky-blue arrows represent model parameters (c_p, t_p, and φ_p) changes from the refence case toward Sets 2, 3, and 5, respectively.

Table 1. *Model Parameters and Emergent Mechanical Properties for the Seven Model Setups presented in Figure 3*

	Model parameters		Emergent Mohr-Coulomb parameters		Final state
	c_p and t_p [MPa]	φ_p [°]	*c* [MPa]	ϕ [°]	
Set 1	2.17	17	0.63	34.0	stable
Set 2	1.91	17	0.58	34.1	unstable
Set 3	2.17	16	0.64	33.3	unstable
Set 4	1.59	21	0.38	36.9	stable
Set 5	2.65	15	0.89	32.2	stable
Set 6	0	23	0.05	38.5	unstable
Set 7	5.83	2	3.8	10.8	unstable

3.1.2 Stability domain

The respective domains of stability and instability that we identified based on the SR method are shown in Figure 3, defined as functions of c and ϕ. Seven simulation setups were used to determine these domains based on the volcano's behavior. The local (c_p, t_p, and φ_p) and emergent (c and ϕ) mechanical properties corresponding to these seven setups are specified in Table 1. All the simulations were run during the same number of iterations and stability was assessed at the same final iteration it_{max}. According to our results, the volcano remains stable above the red line but becomes unstable at and below this limit. As expected, the instability limit shows an inverse relationship between c and ϕ, implying that a decrease in cohesion must be compensated by an increase of friction to counterbalance the shear strength and ensure the stability.

To better understand how our synthetic volcano behaves, we analyze three representative cases (Sets 3, 6, and 7) lying along the stability limit (Figure 4). Although all three cases lead to unstable behaviors, they exhibit distinct deformation patterns depending on the values of c and ϕ.

For low cohesion and high friction angle (Set 6), the behavior is close to that of a cohesionless (i.e., purely frictional) material creeping toward a new stable state: the volcano slides where the topographic slope is steeper than the friction angle and it stabilizes where it is gentler. The magma pressure opens the fracture in a wedge-like manner, with the opening at the upper part being larger than at depth. Consequently, the volcano surface becomes steeper and the amplitude of the deformation is higher for the upper parts close to the volcano summit (Figure 4g-i). A rock volume, whose base is located at a depth of about 500 m, is affected by displacements higher than 3 m. However, this destabilization does not lead to a total collapse of the summit but rather to superficial movements associated to the sliding of a layer with a maximal thickness of about 150 m (Figure 4h). As a result of the fracture location, slightly off-centered to the NW, and to topographic effects, the W and the S flanks are more affected by the deformation than the N and the E flanks. This asymmetric response is even more remarkable that the magma pressure applies similarly on both walls of the NE-SW fracture (see section 2.2). Additionally, we observe deformation in areas far from the summit, particularly to the North and to the East (Figure 4g). There, the steep relief, combined with the cohesionless nature of Set 6, promotes superficial deformation (see section 4.1 for further discussion).

For high cohesion and low friction angle (Set 7), the destabilization is more evident and pronounced (Figure 4j-l). Indeed, the volcano is inherently more stable due to the higher cohesion of its constitutive material. When the magmatic pressure breaks the rock material, the remaining strength is only due to frictional effects and, because the friction angle is much smaller (10.8°) than the topographic slope (higher than 40° above 2000 m asl), the collapse is catastrophic (i.e., brittle). The SW half of the volcano summit collapses and the displacement amplitudes of the three upper marker particles exceed 300 m. As shown in the corresponding cross section, this displacement is effective up to 1,000 m below the summit.

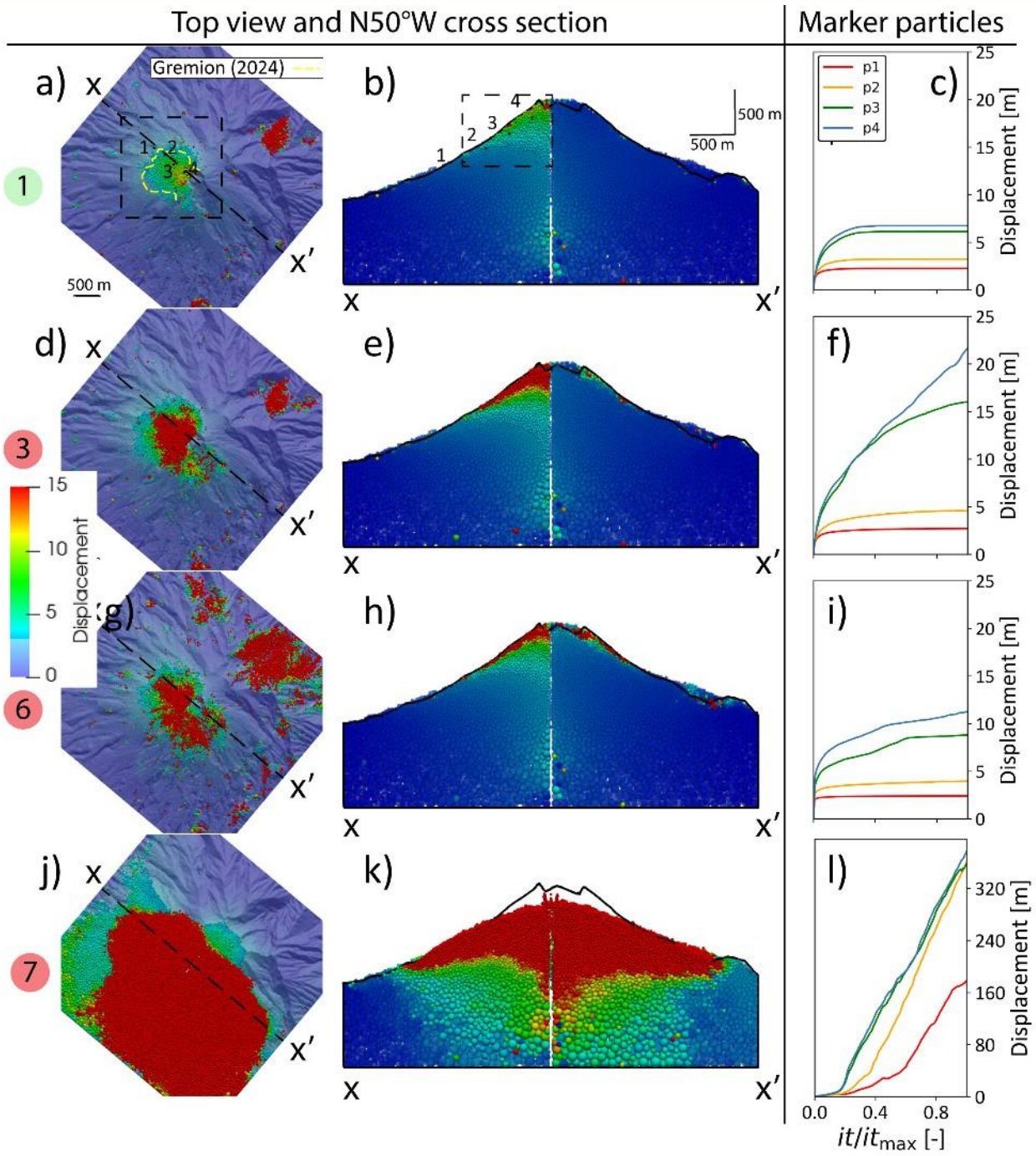

Figure 4. Top views and x-x' cross sections of the displacement fields at the ends of the simulations (it/it_{max} = 1) for different parameter sets (see Table 1 for the parameters): (**a**-**c**) Set 1 is stable at the end of the simulation while (**d**-**l**) Sets 3, 6 and 7 are unstable. Particles with displacements greater than 3 m are shown in solid color, while those with displacements below 3 m are rendered with partial opacity. The locations of the marker particles, the deformed zone identified by Grémion (2024), and the black dashed squares indicating the zoomed-in regions used later in Figure 7 are shown in (**a**) and (**b**). On the right (**c**, **f**, **i,** and **l**), the displacements of marker particles are shown relative to their positions just before the onset of fracture pressurization at it/it_{max} = 0.

For the intermediate values of Set 3 (Figure 4d-f), the behavior is very close to that observed with Set 6. However, this set of parameters gives a deformation more restricted to the NW flank and closer to the one observed in the field. Nonetheless, because the amplitude of the deformation is higher than the one observedin the field (>12 m on Figure 4f without deceleration after 20 m of displacement), Set 3 lies in the instability domain.

In contrast to the unstable Sets 3, 6, and 7, Set 1 reproduces the stability-like state following the flank destabilization observed during the 2020-2021 crisis (Figure 1 and 4c). Additionally, this set produces the displacements that most closely match those measured at Merapi, not only in terms of displacement amplitudes but also in terms of spatial extent of the mobilized zone (Figure 4a-c). Thus, Set 1 is chosen as our reference case, lying in the stability domain of Figure 3.

3.2 Reference case

The back analysis enabled us to determine a set of representative mechanical properties for Merapi volcano (Set 1). In the following, we analyze the response of the model setup with these properties in terms of kinetics and kinematics, and also present a parametric study to assess how changes of mechanical properties influence the simulated behavior.

3.2.1 Kinetics: ascending magma column

During the 2020-2021 crisis, the progressive increase of the deformation observed over several months could be due to a progressive increase of the force exerted by the magma on the fracture walls, because the fracture has grown, and/or because the pressure has increased when the magma rose up until it was able to erupt on the surface of the volcano (i.e., lava domes growth, Figure 1). Here, in order to get insights into the kinetics of the instability, we thus simulate the progressive ascent of the magma and the associated pressurization of the fracture. We assume that the magma column starts from 1,765 m, an elevation sufficiently deep that no significant summit deformation is detected by magma pressurization, and that it ascends up to 2,855 m, corresponding to the elevation of the 2021 crater dome. Note that the overpressure is only applied after the magma reaches the crater surface (2,805 m) to simulate the lava domes growth.

The displacement evolution of a DE located at the Rb1 reflector position is shown in Figure 5 (Rb1 located on Fig. 1a). Note that this DE undergoes larger displacement amplitudes than those shown in Figure 4c, as it lies on the topographic surface of the volcano and not 100 m below it.

Three key aspects characterize the deformation:

1. The deformation is small when the top of the magma column is below an elevation of 2,700 m and then it increases exponentially. Most of the deformation occurs when the magma goes over the crater floor (2,805 m), in correlation with the dome growth. At the end of the magma ascent (the lava domes stop to grow), the displacement amplitude

projected in the BAB observatory direction reaches approx. 8 m, which is slightly less than the 10 m measured by the BPPTKG in June 2021 (Figure 1).

2. The deformation is mainly inelastic (results from plastic processes) as highlighted by the additional unloading phase that we performed at the end of the simulation where we made the pressure falls back from the top of the dome (2,855 m) to 2,750 m (lowest point of the summit crater). We can see that the pressure drop has very little effect on the displacement of the reflector (Fig. 5).
3. As observed in the field, the system reaches a new equilibrium state at the end of the loading, despite the inelastic response of the system. The flank seems to have simply adjusted its geometry to the loading but did not suffer any catastrophic failure.

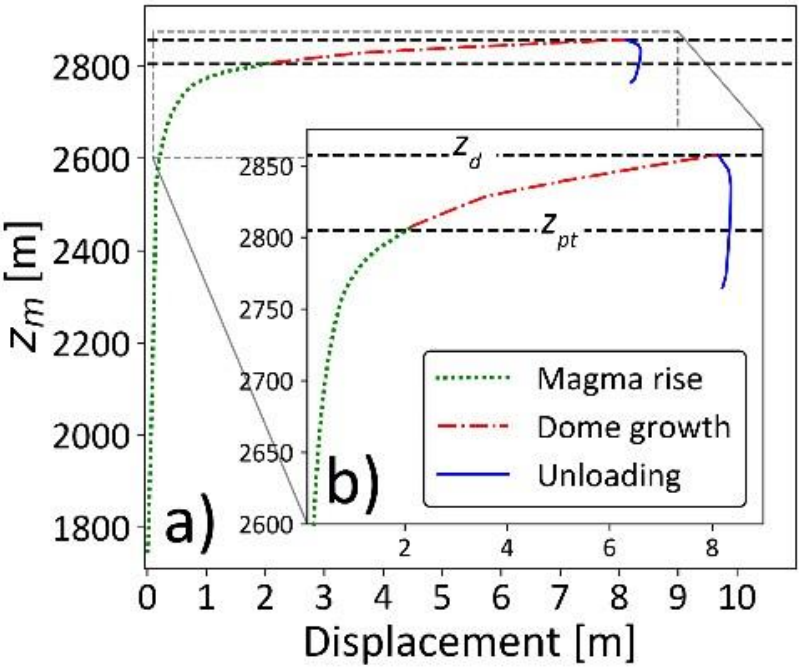

Figure 5. (**a**) Evolution of the displacement, projected along the direction of the BAB observatory, of a DE located at the RB1 reflector position on the NW flank of the model, as a function of the magma column height z_m during the magma rise in the fracture, pressure increase related to dome growth, and unloading phases. (**b**) Zoom into the exponential increase shown in (a). z_{pt} and z_d refer to the crater floor (2010 plateau top at 2,805 m) and the 2021 dome summit elevations (2,855 m), respectively, and are represented with horizontal dashed lines.

3.2.2 Kinematics: Deformation and extents

As shown in Figure 4b, the deformation is not limited to the flank surface but involves a volumetric domain extending over ~500 m vertically and covering approximately 1 km² on the NW flank of the volcano. The deformation map evidences a wedge whose base is located at around 500 m below the summit, intersecting the flank surface at the elevation of marker p2. In total, a mobilized and subsequently stabilized volume of approximately 116 million m³ has moved by more than 3 m. Below this wedge, the deformation is effective but limited and tends to diminish with depth. At greater depths, some substantial deformation can be seen close to the fracture (approx. 1,500 m below the summit) but this is most probably related to the adaptative mesh which tends to favor larger porosities in areas where larger DEs are packed (below 800 m).

Looking at the displacement field on the mobilized wedge (Figure 6), the deformation directly results from the pressure applied on the NE-SW fracture as evidenced by the horizontally oriented displacement vectors. At the RB1 location, the total displacement consists of roughly 80% horizontal and 20% vertical components. From the marker particles recordings (Figure 4) and the displacement vectors in Figure 6, we can see that the displacement amplitude increases when getting closer to the summit, evidencing a displacement gradient over the flank. Moreover, the displacements show vertical components on the upper part of the mobilized volume which suggest an overall tilting of the summit due to the magma pressure: upwardly close to the fracture and downwardly close to the free surface of the volcano flank. One can note that this tilting is opposite to what is typically observed in rotational slidings, which characterizes many volcano flank collapses.

3.2.3 Sensitivity analysis

To better assess the influence of the properties of the edifice on its response to the pressurization, we show in Figure 7 how small variations in mechanical properties can affect the overall deformation.

Firstly, we compare, in Figures 7a, b and c, the reference stable Set 1 with unstable Sets 2 and 3, which local strengths c_p and t_p, and interparticle friction angles φ_p only differ by 0.1 MPa and 1°, respectively (see Table 1). It can be seen that a slight reduction of the plastic properties, related to the material strength, increases the extent of the deformation, both horizontally and vertically. Furthermore, it causes instabilities in the upper part of the flank as evidenced by the greater increase in displacement around z = 2,500-2,600 m for Sets 2 and 3 compared to the reference stable Set 1 (Figure 7c). Above this height, an unstable and still moving 200 m depth layer, with displacements and velocities greater than our stability thresholds (displacement > 10 m without deceleration), is observed. For Set 3, this unstable layer corresponds to the upper zone represented in red in Figure 4e.

Secondly, we compare in Figures 7d, e and f, the reference stable Set 1 with two additional sets, 8 and 9, which present the same strength parameters but different elastic properties (i.e., Young's modulus, *E*, related to the material stiffness). It is shown that increasing *E* by a factor of 1.25 (Set 8) does not change the extent of the deformation. However, it amplifies the wedge movement as illustrated by the displacement which reaches up to 30 m at an altitude of 2,700 m. This increase of stiffness thus favors instability. Conversely, a decrease of *E* by a factor of 0.75 (Set 9), increases the extent of the deformation, both horizontally and vertically, as well as the amplitude of the displacement as illustrated by the displacement which reaches up to 10 m at an altitude of 2,700 m. However, contrary to the stiffer case, this "softer" version of the volcano remains stable, even though it experienced larger deformation.

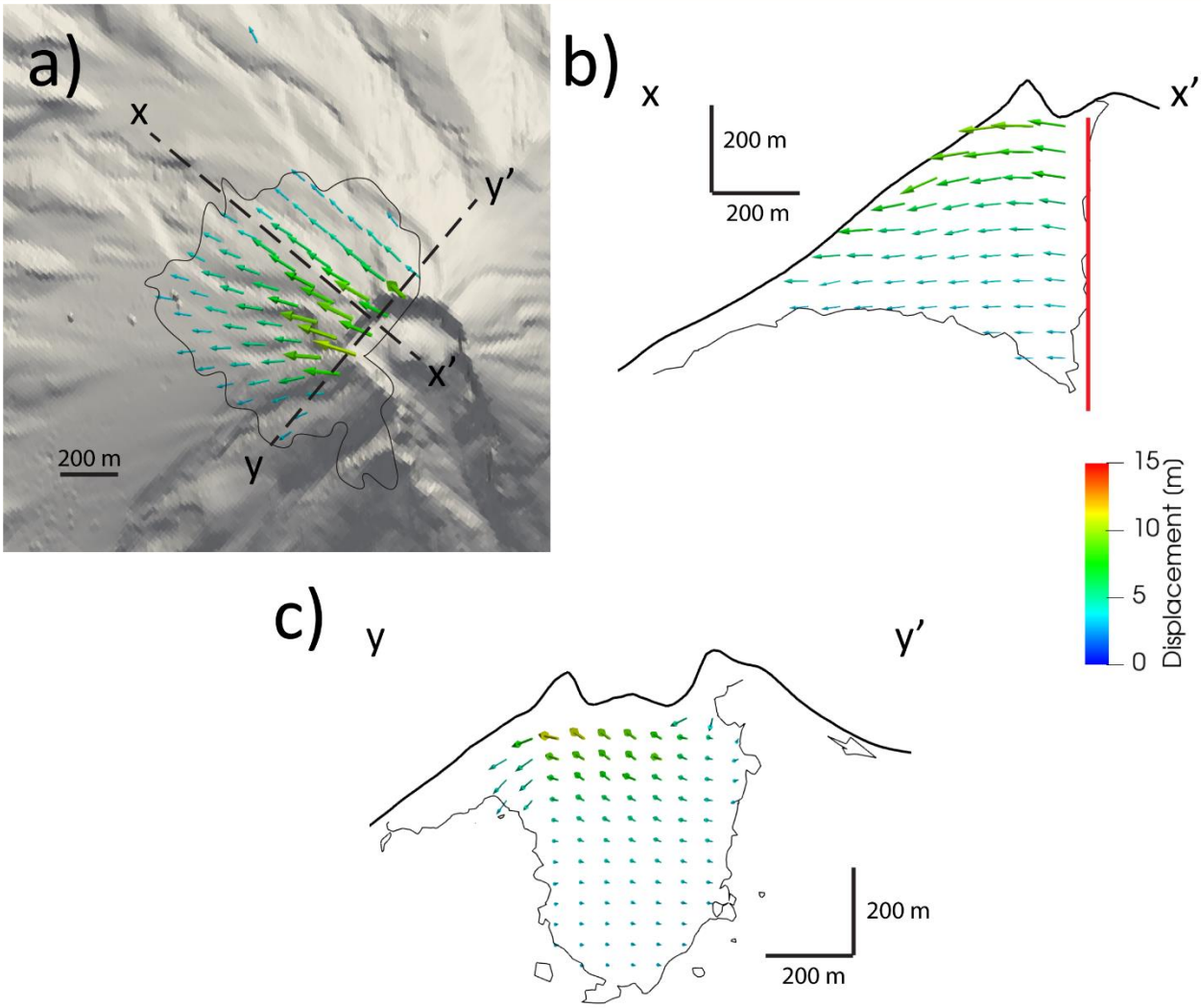

Figure 6. (**a**) Top view showing the displacement vector field of the reference case (Set 1 in Table 1). (**b**-**c**) Cross sections showing the vertical distribution of the displacement vector field respectively perpendicular and parallel to the fracture plane within the zones identified by the black dashed squares shown in Figure 4a-b. Only displacements greater than 3 m are shown. The thin black contour delimits the area that experienced displacements bigger than 3 m. The fracture is represented by the red line in Figure 6b.

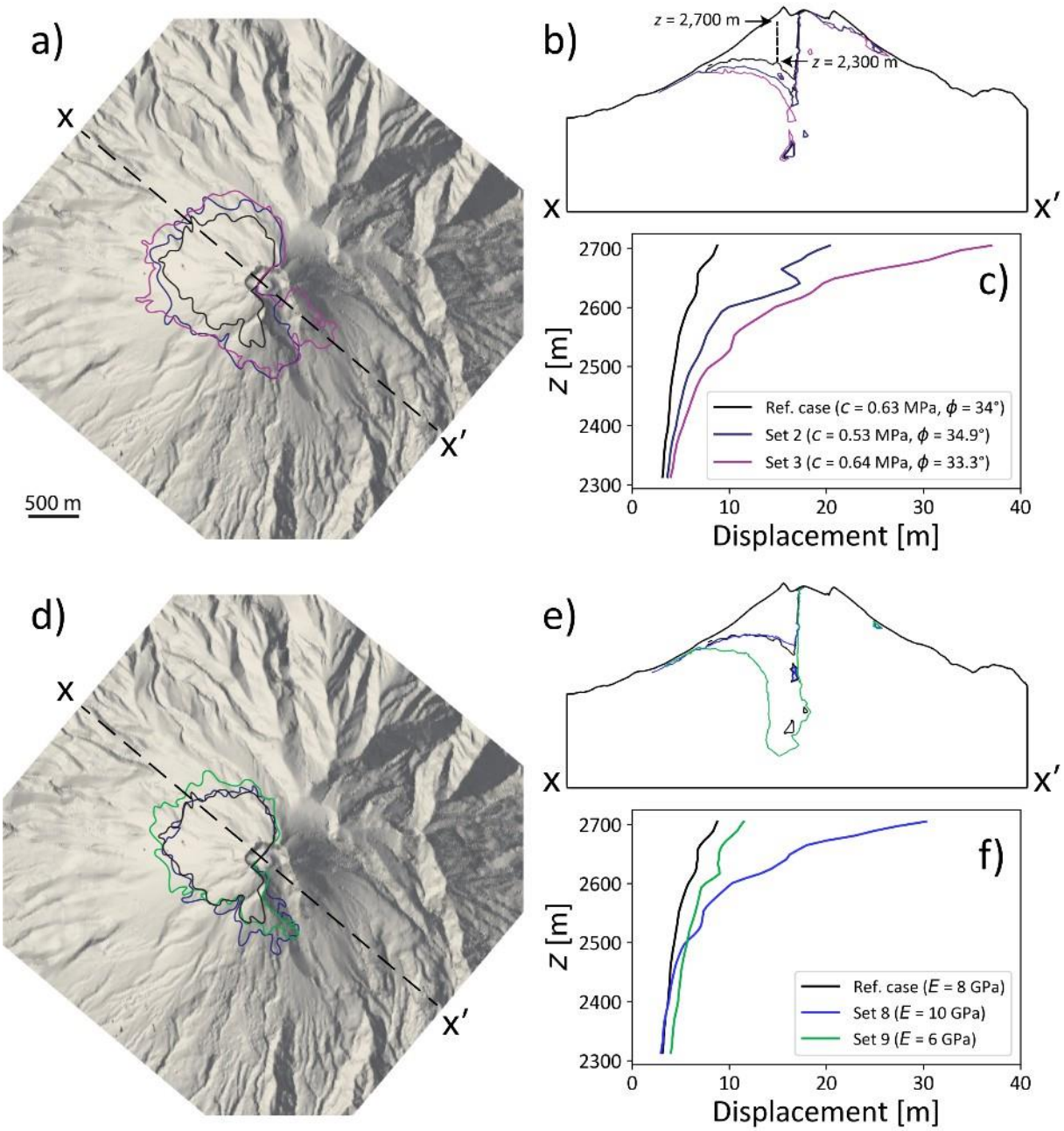

Figure 7. Influence of the mechanical properties of the edifice on the pressure induced deformation of the synthetic volcano. Top figures: contours delimiting the more than 3 m displacements for the reference case (Set 1) and Sets 2 and 3 which have different plastic properties: (**a**) top view, (**b**) NW-SE cross section, and (**c**) displacement profiles along the volcano upper part, from z = 2,300 to z = 2,700 m. Bottom figures: contours delimiting the more than 3 m displacements for the reference case (Set 1) and Sets 8 and 9 which have different elastic properties: (**d**) top view, (**e**) NW-SE cross section, and (**f**) displacement profiles along the volcano upper part, from z = 2,300 to z = 2,700 m.

4. Discussion

4.1 Limitation of the model

Obviously, we had to make several simplifying assumptions to perform our numerical analysis. For instance, our synthetic volcano is considered as a homogeneous medium, the magma pressure distribution is magma-static and applied along a planar fracture plane, and pore pressure and thermal effects are not taken into account while they can affect stability through induced effective stress changes (Voight & Elsworth, 1997).

As mentioned in section 2.3, the Merapi stratovolcano is characterized by alternating lava flows, pyroclastic layers, lahar deposits, as well as lava domes, all overprinted by erosion. Although heterogeneities can be explicitly incorporated into DEM models (e.g., Lu et al., 2018; Scholtès & Donzé, 2012), field constraints are not sufficiently accurate to characterize them beneath the surface. As a result, we can only study the global behavior of Merapi considering average mechanical properties. This is also why, for low cohesion values, large superficial displacements can be observed in areas not affected by the magma pressurization: they are characterized by steep slopes or cliffs not compatible with the mechanical properties (see Figure 4g). One can note that, overall, our reference case presents mechanical properties (c = 0.6 MPa and ϕ = 34°) that are consistent with both the summit topographic slope angle and the fractured cliffs located on the summit crater (Beauducel et al., 2000, 2006).

Magma generally flows within complex geometries influenced by conduit erosion or by accretion of magma (de' Michieli Vitturi et al., 2008). Simplified fracture geometries are commonly used in numerical modeling of volcanoes, mainly in inversion modeling (e.g., Bonforte & Guglielmino, 2015). However, more complex conduit geometries (e.g., transition from an elliptic dyke to a cylindrical conduit, presented in Hautmann et al., 2009) can be used. In our simulations, the magma flows within a vertical fracture plane with a constant geometry (i.e., aperture and width). This is clearly an oversimplification that can affect magma ascent dynamics and, consequently, the pressure induced deformation. One can note however that our results indicate that flank deformations only become significant when the magma exceeds the Merapi's crater height, over around 2,700 m (Figure 5). This would suggest that considering a more complex conduit geometry below the crater floor would not drastically change our conclusions. Nevertheless, conduit geometry plays a key role in controlling deformation, as discussed in section 4.3. In addition, although DEM models can explicitly deal with progressive fracture propagation (Scholtès & Donzé, 2012), we did not include this possibility in our model because of the added complexity to parametrize the model without field data. Instead, we considered the final geometry of the NE-SW fracture, inferred from field observations.

Three pressure terms are usually defined when magma flow is considered to be the cause of volcanic deformation: magma-static normal stress, viscous shear stress, and overpressure terms that can be related either to the magma composition, tectonic stresses and/or magma chamber processes (Beauducel et al., 2000; Marsden et al., 2019; Nishimura, 2009). Given that there was no evidence of magma flow during the 2020-2021 crisis (Grémion, 2024), we did not introduce the effect of shear stress in our simulations and only considered quasi static pressure

loadings (i.e., magma-static normal stress and an overpressure term related to the summit domes growth). Adding the contributions of other pressure terms would probably affect the stability of our synthetic volcano (i.e., different critical properties; Figure 3) and/or the deformation extent and amplitudes (i.e., larger displacements for similar magma column heights).

Finally, it is worth noting that elastic properties clearly influence the magnitude of pressure induced displacements as well as the stability of our synthetic volcano (see section 3.2.3). For instance, we show that a lower Young's modulus leads to increased deformation amplitudes that can actually quantitatively fit with field observations. According to slope stability studies performed with classical continuous approaches (i.e., FEM models as in Cheng et al., 2007), if elastic properties can influence the amount of deformation prior to failure, they should not drastically change the stability potential of a slope (i.e., factor of safety). Our results suggest otherwise considering local mechanisms that may not be taken into account in global analyses.

4.2 Interpretation of the 2020-2021 crisis

The displacement amplitude of RB1 was measured equal to 10 m in January 2021 and reached 14 m in August (Figure 1). These values correspond well to the range of deformation simulated with our model setup with the parameters of Set 1 (8 m, stable with c = 0.63 MPa and ϕ = 34°), Set 9 (11m, stable with c = 0.63 MPa, ϕ = 34° and a lower E compared to Set 1), and Set 3 (>15 m, unstable with c = 0.64 MPa and ϕ = 33.3°). In terms of spatial extension, these parameter sets also enable to reproduce with good agreement the spatial extent of the destabilized zone observed on Merapi's NW flank (Figure 4; Grémion, 2024). Finally, as observed in the field, the deformation stops at the end of the loading, when magma pressure cannot increase further up because the domes have reached their maximum heights. Based on these similarities, we can thus propose an interpretation of the 2020-2021 crisis based on our results.

Firstly, the model demonstrates that the overpressure inferred from the dome height (1.2 MPa) is sufficient to produce a surface deformation close to that observed in the field. The model also shows that the magma pressure opened the fracture in a wedge-like manner: the higher the elevation, the wider the fracture, with its opening reaching up to 10 meters at the crater floor. The pressure-induced deformation pushes and steepens the upper slopes of the NW flank. Given the relatively low cohesion and high friction angle of the material, surface rocks (to a depth of approximately 200 m) fail and slide downslope. This is actually consistent with the large (>100 m) collapses observed on the crater walls, as well as with the rock dismantling and sliding observed on Merapi's NW flank during the crisis. Our results also reveal that the shape and the location of the fracture play a key role in determining the localization of the deformation. Indeed, because it is slightly off-centered toward the northwest of the crater, only the NW flank is affected by the magma pressurization, while the other flanks remain stable. Finally, and more critically, our study reveals that the deformation is not restricted to the surface of the volcano: a 500 m deep portion of Merapi's flank comprising 116 million m^3 of rock could have been mobilized during the 2020-2021 crisis.

According to the field data (Figure 1), there were two phases of deformation: from November 2020 to January 2021 and then from June to August 2021. We did not manage to model the second phase with our model setup. The interruption from January to June 2021 is

probably linked to a drop in pressure when the lava flowed to the surface to form the two domes. The resumption of deformation in June seems to be linked to the increase in pressure in the magma system associated with the thickening of the domes (from 50 m to 75 m; Grémion, 2024). It might also be due to internal changes which cannot be related to observations (e.g., internal fracture propagation, thermo-hydromechanically induced damage, etc.). A key result of our model however concerns the kinetics of the first phase of deformation. As shown in Figure 5, the deformation increases exponentially with a magma overpressure corresponding to magma column heights higher than the crater floor elevation (2,805 m). This asymptotic trend resembles the temporal evolution of deformation measured during the 2020-2021 crisis (Figure 1b). By comparing the two curves, we can assume that the magma level was at approximately 2,000 m elevation in July 2020, when deformation was first detected, and had reached the crater floor at 2,805 m in January. Assuming a constant ascent rate of magma within the fracture, this comparison suggests a vertical velocity of about 3.83 m/day, which, associated to a fracture length of 450 m and an average width of 10 m, corresponds to a volumetric rate of roughly 17,000 m^3/day. Even though resulting from simplifications, this value is remarkably close to the mean extrusion rate estimated for both 2021 crater and flank domes (18,000 m^3/day; Grémion, 2024). This effusion rate, in turn, is four times higher than the one estimated for the 2018-2019 lava dome (3,000-4,000 m^3/day as specified according to Grémion et al., 2023 and Kelfoun et al., 2021), and also exceeds the long-term average eruption rate over the past century, estimated at 0.10×10^6 m^3/month (i.e., ~3,300 m^3/day) by Siswowidjoyo et al. (1995).

4.3 Implications for the stability of Merapi

Generally, magma at Merapi erupts through a conduit a few tens of meters long, circular or elongated, and located near the center of the crater. For instance, Beauducel et al. (2000) modeled the 1993-1997 summit deformation at Merapi volcano using a 25-m radius cylindrical conduit as the deformation source. With such a geometry and for a pressure consistent with the height of the lava dome, ground deformation would be limited compared to what was observed during the 2020-2021 crisis. Indeed, considering the same vertical pressure distribution, the resultant force produced by a 25-m radius pressurized cylindrical conduit would correspond to approximately 17% of the force exerted by the NE-SW fracture we considered. Hence, unreasonable high pressure values (a ~300 m thick lava dome) would be required to produce forces comparable to those simulated with the fracture. Our results thus suggest that, to reproduce the sliding and dismantling observed during the 2020-2021 crisis, a dike (pressurized fracture) needs to be considered as the deformation source. Intrusion induced flank deformations have been observed at many volcanoes around the world (Bonforte & Guglielmino, 2015; Elsworth & Day, 1999), and it should thus not come as a surprise in the context of the Merapi volcano. Furthermore, two conditions must be fulfilled: (1) the fracture must be located closer to the northwestern flank than to the southeastern flank, and (2) the fracture must be long enough, comparable to the width of the summit area, to produce the necessary driving force. The reason why the fracture was formed close to the northwestern flank in 2020 remains unknown (e.g., local stress rotation, heterogeneities, pre-existing planes of weakness, ...) but there is no reason to exclude the possibility that another fracture could form somewhere else in the future and that it could then shift the deformation to another area/flank.

As confirmed by our results, Merapi volcano seemed to have adjusted its geometry to the magma loading as it eventually reached a new equilibrium state at the end of the 2020-2021 crisis. This adjustment involved inelastic processes at depth but it did not produce a large-scale flank collapse such as that of Mount St. Helens. According to our models and based on our assumptions, such a catastrophic collapse could only have occurred if the rock material presented a relatively high cohesive (brittle) nature, as illustrated in Figure 4. Considering the predominantly frictional nature of Merapi's rock material inferred from our back analysis, only a sudden drop in friction (caused by physicochemical alteration processes) or effective stress variations (caused by thermo-hydro-mechanically induced pore pressure buildups) could eventually lead to a catastrophic failure. All these phenomena are present within volcanic edifices and cannot thus be ruled out. That is why, in the future and despite our conclusions, we cannot exclude a catastrophic collapse to occur at Merapi. Future works could thus consist in building upon our models (or the mechanical properties we inferred) to assess the role of these phenomena on Merapi's stability.

5. Conclusions

We developed discrete element method (DEM) models to investigate the flank instability observed at Merapi during the 2020–2021 crisis. The simulations were performed assuming a simplified, homogeneous mechanical behavior of the volcanic edifice, with magma overpressure applied along the NE-SW-trending fracture identified during the crisis. Despite these simplifying assumptions, a back-analysis approach allowed us to determine a set of effective bulk mechanical properties capable of reproducing the deformation observed on the NW flank of the volcano, both qualitatively and quantitatively.

The results indicate that the deformation was not limited to the flank surface but involved a volumetric domain extending over approximately 500 m in vertical extent and covering about 1 km^2 on the NW side of the edifice. In total, a mobilized volume of approximately 116 million m^3 may have undergone displacements exceeding 3 m in response to magma pressurization, before subsequently stabilizing. As documented by field observations, the pressure-induced deformation did not culminate in a catastrophic flank collapse; instead, it resulted in progressive creep of the volcanic flank toward a new equilibrium configuration.

Our analysis suggests that the observed deformation is governed by inelastic processes that developed predominantly in the upper part of the edifice, where confining stresses are lower and the relative influence of magma pressure is higher. Pressure forces acting along the fracture walls induced a slight tilting of the northwestern flank, leading to downslope sliding with displacement magnitudes increasing with elevation. This sliding process ceased once pressurization diminished and the flank topography adjusted accordingly.

Decametric-scale collapses and progressive dismantling of a volcanic flank are particularly concerning phenomena, as they may be interpreted as precursors to catastrophic flank failure and debris-avalanche formation. In this context, the 2020-2021 Merapi crisis is noteworthy, as it illustrates how magma-pressure-driven topographic readjustments can generate substantial deformation without triggering large-scale instability. By successfully reproducing the observed

deformation patterns and providing a coherent mechanical interpretation of the underlying processes, the DEM approach emerges as a particularly promising tool for anticipating the evolution of similar volcanic crises. Future work will focus on incorporating additional complexity into the modeling framework, including material heterogeneity (e.g., pre-existing faults or mechanical contrasts) and multiphysical processes (e.g., thermos-hydro-mechanical coupling), in order to further constrain the mechanisms controlling volcanic flank deformation.

Acknowledgments

This work was carried out as part of the first author's PhD project, funded by the ClerVolc research institute through a PhD scholarship. The authors would like to thank William Guyot-Lénat and the ISIMA institute at the Université Clermont Auvergne for providing the computational resources used in this study. The authors also thank the reviewers for their comments and suggestions which helped us to improve the manuscript. This is the contribution no. 737 of the ClerVolc program of the International Research Center for Disaster Sciences and Sustainable Development of the Université Clermont Auvergne.

Open Research

Data provided by the BPPTKG (Balai Penyelidikan dan Pengembangan Teknologi Kebencanaan Geologi) – CVGHM (Center for Volcanology and Geological Hazard Mitigation) were used to constrain our models. These data, along with example simulation input files, and the simulation corresponding scripts, are available in Galárraga et al. (2026). The stereoscopic images of Merapi, including but not limited to the 2020 instability crisis period, are available in Kelfoun (2023). These summit images were obtained as part of the VELI Instrumented Site (IRD). The main numerical modeling software used in this study is YADE (Angelidakis et al., 2024; Smilauer et al., 2021), an open-source discrete element method (DEM) code. Figures were made with Matplotlib version 3.7.1 (Caswell et al., 2023). Displacement maps and renderings were produced using ParaView version 5.12 (Ahrens et al., 2005).

Conflict of Interest Statement

The authors have no conflicts of interest to disclose.

References

Acocella, V. (2005). Modes of sector collapse of volcanic cones: Insights from analogue experiments: ANALOGUE MODELS OF VOLCANO COLLAPSE. *Journal of Geophysical Research: Solid Earth*, *110*(B2). https://doi.org/10.1029/2004JB003166

Ahrens, J., Geveci, B., & Law, C. (2005). 36 - ParaView: An End-User Tool for Large-Data Visualization. In C. D. Hansen & C. R. Johnson (Eds.), *Visualization Handbook* (pp. 717–731). Burlington: Butterworth-Heinemann. https://doi.org/10.1016/B978-012387582-2/50038-1

Albino, F., Pinel, V., Massol, H., & Collombet, M. (2011). Conditions for detection of ground deformation induced by conduit flow and evolution. *Journal of Geophysical Research: Solid Earth*, *116*(B6). https://doi.org/10.1029/2010JB007871

Angelidakis, V., Boschi, K., Brzeziński, K., Caulk, R. A., Chareyre, B., del Valle, C. A., et al. (2024). YADE - An extensible framework for the interactive simulation of multiscale, multiphase, and multiphysics particulate systems. *Computer Physics Communications*, *304*, 109293. https://doi.org/10.1016/j.cpc.2024.109293

Apuani, T., Corazzato, C., Merri, A., & Tibaldi, A. (2013). Understanding Etna flank instability through numerical models. *Journal of Volcanology and Geothermal Research*, *251*, 112–126. https://doi.org/10.1016/j.jvolgeores.2012.06.015

Beauducel, F., Cornet, F., Suhanto, E., Duquesnoy, T., & Kasser, M. (2000). Constraints on magma flux from displacements data at Merapi volcano, Java, Indonesia. *Journal of Geophysical Research: Solid Earth*, *105*(B4), 8193–8203.

Beauducel, F., Nandaka, M. A., Cornet, F. H., & Diament, M. (2006). Mechanical discontinuities monitoring at Merapi volcano using kinematic GPS. *Journal of Volcanology and Geothermal Research*, *150*(1), 300–312. https://doi.org/10.1016/j.jvolgeores.2005.07.005

Bemelmans, M. (2025). *Volcano monitoring with high-resolution satellite SAR* (Doctoral dissertation). Retrieved from University of Bristol Research Information Repository (https://research-information.bris.ac.uk/en/studentTheses/volcano-monitoring-with-high-resolution-satellite-sar). Bristol, United Kingdom: University of Bristol.

Bonforte, A., & Guglielmino, F. (2015). Very shallow dyke intrusion and potential slope failure imaged by ground deformation: The 28 December 2014 eruption on Mount Etna. *Geophysical Research Letters*, *42*(8), 2727–2733. https://doi.org/10.1002/2015GL063462

Bonilla-Sierra, V., Scholtès, L., Donzé, F. V., & Elmouttie, M. K. (2015). Rock slope stability analysis using photogrammetric data and DFN–DEM modelling. *Acta Geotechnica*, *10*(4), 497–511. https://doi.org/10.1007/s11440-015-0374-z

Bozzano, F., Gaeta, M., Lenti, L., Martino, S., Paciello, A., Palladino, D. M., & Sottili, G. (2013). Modeling the effects of eruptive and seismic activities on flank instability at Mount Etna, Italy. *Journal of Geophysical Research: Solid Earth*, *118*(10), 5252–5273. https://doi.org/10.1002/jgrb.50377

Casagli, N., Tibaldi, A., Merri, A., Del Ventisette, C., Apuani, T., Guerri, L., Fortuny-Guasch, J., & Tarchi, D. (2009). Deformation of Stromboli Volcano (Italy) during the 2007 eruption revealed by radar interferometry, numerical modelling and structural geological field data. *Journal of Volcanology and Geothermal Research*, *182*(3), 182–200. https://doi.org/10.1016/j.jvolgeores.2009.01.002

Caswell, T. A., Lee, A., Andrade, E. S. de, Droettboom, M., Hoffmann, T., Klymak, J., et al. (2023, March 4). matplotlib/matplotlib: REL: v3.7.1 [Software]. Zenodo. https://doi.org/10.5281/zenodo.7697899

Cayol, V., & Cornet, F. H. (1998). Effects of topography on the interpretation of the deformation field of prominent volcanoes—Application to Etna. *Geophysical Research Letters*, *25*(11), 1979–1982. https://doi.org/10.1029/98GL51512

Cecchi, E., van Wyk de Vries, B., & Lavest, J.-M. (2004). Flank spreading and collapse of weak-cored volcanoes. *Bulletin of Volcanology*, *67*(1), 72–91. https://doi.org/10.1007/s00445-004-0369-3

Cheng, Y. M., Lansivaara, T., & Wei, W. B. (2007). Two-dimensional slope stability analysis by limit equilibrium and strength reduction methods. *Computers and Geotechnics*, *34*(3), 137–150. https://doi.org/10.1016/j.compgeo.2006.10.011

Criswell, C. W. (1987). Chronology and pyroclastic stratigraphy of the May 18, 1980, Eruption of Mount St. Helens, Washington. *Journal of Geophysical Research: Solid Earth*, *92*(B10), 10237–10266. https://doi.org/10.1029/JB092iB10p10237

Cundall, P. A., & Strack, O. D. L. (1979). A discrete numerical model for granular assemblies. *Géotechnique*, *29*(1), 47–65. https://doi.org/10.1680/geot.1979.29.1.47

Currenti, G., Bonaccorso, A., Del Negro, C., Scandura, D., & Boschi, E. (2010). Elasto-plastic modeling of volcano ground deformation. *Earth and Planetary Science Letters*, *296*(3), 311–318. https://doi.org/10.1016/j.epsl.2010.05.013

Del Negro, C., Currenti, G., & Scandura, D. (2009). Temperature-dependent viscoelastic modeling of ground deformation: Application to Etna volcano during the 1993–1997 inflation period. *Physics of the Earth and Planetary Interiors*, *172*(3), 299–309. https://doi.org/10.1016/j.pepi.2008.10.019

Diederichs, M. S., Lato, M., Quinn, P., & Hammah, R. (2007). Shear strength reduction approach for slope stability analyses (p. ARMA-07). Presented at the ARMA Canada-US Rock Mechanics Symposium, ARMA.

Donnadieu, F., Merle, O., & Besson, J.-C. (2001). Volcanic edifice stability during cryptodome intrusion. *Bulletin of Volcanology*, *63*(1), 61–72. https://doi.org/10.1007/s004450000122

Duriez, J., Scholtès, L., & Donzé, F.-V. (2016). Micromechanics of wing crack propagation for different flaw properties. *Engineering Fracture Mechanics*, *153*, 378–398. https://doi.org/10.1016/j.engfracmech.2015.12.034

Elsworth, D., & Day, S. J. (1999). Flank collapse triggered by intrusion: The Canarian and Cape Verde Archipelagoes. *Journal of Volcanology and Geothermal Research*, *94*(1), 323–340. https://doi.org/10.1016/S0377-0273(99)00110-9

Galárraga, M., Scholtès, L., Chevalier, B., Aisyah, N., & Kelfoun, K. (2026). *Example simulation of Merapi volcano flank deformation* [Dataset]. Zenodo. https://doi.org/10.5281/zenodo.18428576

Gertisser, R., Charbonnier, S. J., Keller, J., & Quidelleur, X. (2012). The geological evolution of Merapi volcano, Central Java, Indonesia. *Bulletin of Volcanology*, *74*(5), 1213–1233. https://doi.org/10.1007/s00445-012-0591-3

Gertisser, R., del Marmol, M.-A., Newhall, C., Preece, K., Charbonnier, S., Andreastuti, S., et al. (2023). Geological History, Chronology and Magmatic Evolution of Merapi (pp. 137–193). https://doi.org/10.1007/978-3-031-15040-1_6

Global Volcanism Program. (2021). *Report on Merapi (Indonesia)* (Monthly Bulletin Report No. 46:3). Smithsonian Institution. https://doi.org/10.5479/si.GVP.BGVN202103-263250

Green, D. N., Neuberg, J., & Cayol, V. (2006). Shear stress along the conduit wall as a plausible source of tilt at Soufrière Hills volcano, Montserrat. *Geophysical Research Letters*, *33*(10). https://doi.org/10.1029/2006GL025890

Grémion, S. (2024). *Potentiel de l'imagerie satellitaire pour la surveillance des stratovolcans andésitiques, exemple du volcan Mérapi (Indonésie)* (Doctoral dissertation). Retrieved from theses.fr (https://theses.fr/s295667). Chambéry, France: Université Savoie Mont Blanc.

Grémion, S., Pinel, V., Shreve, T., Beauducel, F., Putra, R., Solikhin, A., et al. (2023). Tracking the evolution of the summit lava dome of Merapi volcano between 2018 and 2019 using DEMs derived from TanDEM-X and Pléiades data. *Journal of Volcanology and Geothermal Research*, *433*, 107732. https://doi.org/10.1016/j.jvolgeores.2022.107732

Harnett, C. E., Heap, M. J., Troll, V. R., Deegan, F. M., & Walter, T. R. (2022). Large-scale lava dome fracturing as a result of concealed weakened zones. *Geology*, *50*(12), 1346–1350. https://doi.org/10.1130/G50396.1

Harnett, C. E., Thomas, M. E., Purvance, M. D., & Neuberg, J. (2018). Using a discrete element approach to model lava dome emplacement and collapse. *Journal of Volcanology and Geothermal Research*, *359*, 68–77. https://doi.org/10.1016/j.jvolgeores.2018.06.017

Hautmann, S., Gottsmann, J., Sparks, R. S. J., Costa, A., Melnik, O., & Voight, B. (2009). Modelling ground deformation caused by oscillating overpressure in a dyke conduit at Soufrière Hills Volcano, Montserrat. *Tectonophysics*, *471*(1), 87–95. https://doi.org/10.1016/j.tecto.2008.10.021

Heap, M. J., Villeneuve, M., Albino, F., Farquharson, J. I., Brothelande, E., Amelung, F., et al. (2020). Towards more realistic values of elastic moduli for volcano modelling. *Journal of Volcanology and Geothermal Research*, *390*, 106684. https://doi.org/10.1016/j.jvolgeores.2019.106684

Heap, M. J., Baumann, T. S., Rosas-Carbajal, M., Komorowski, J.-C., Gilg, H. A., Villeneuve, M., et al. (2021). Alteration-Induced Volcano Instability at La Soufrière de Guadeloupe (Eastern Caribbean). *Journal of Geophysical Research: Solid Earth*, *126*(8), e2021JB022514. https://doi.org/10.1029/2021JB022514

Hickey, J., Gottsmann, J., & del Potro, R. (2013). The large-scale surface uplift in the Altiplano-Puna region of Bolivia: A parametric study of source characteristics and crustal rheology using finite element analysis. *Geochemistry, Geophysics, Geosystems*, *14*(3), 540–555. https://doi.org/10.1002/ggge.20057

Holohan, E. P., Schöpfer, M. P. J., & Walsh, J. J. (2011). Mechanical and geometric controls on the structural evolution of pit crater and caldera subsidence. *Journal of Geophysical Research: Solid Earth*, *116*(B7). https://doi.org/10.1029/2010JB008032

Hoek, E., & Diederichs, M. S. (2006). Empirical estimation of rock mass modulus. *International Journal of Rock Mechanics and Mining Sciences*, *43*(2), 203–215. https://doi.org/10.1016/j.ijrmms.2005.06.005

Huber, M., Scholtès, L., & Lavé, J. (2024). Stability and failure modes of slopes with anisotropic strength: Insights from discrete element models. *Geomorphology*, *444*, 108946. https://doi.org/10.1016/j.geomorph.2023.108946

Jensen, E. K., & Moore, J. R. (2023). Coevolution of Rock Slope Instability Damage and Resonance Frequencies From Distinct-Element Modeling. *Journal of Geophysical Research: Earth Surface*, *128*(11), e2023JF007305. https://doi.org/10.1029/2023JF007305

Kavanagh, J. L., Engwell, S., & Martin, S. (2017). A review of analogue and numerical modelling in volcanology. *Solid Earth Discussions*. Retrieved from http://dx.doi.org/10.5194/se-2017-40

Kelfoun, K. (2023). StereoVolc [Dataset]. OPGC, LMV. https://doi.org/10.25519/STEREOVOLC

Kelfoun, K., Santoso, A. B., Latchimy, T., Bontemps, M., Nurdien, I., Beauducel, F., et al. (2021). Growth and collapse of the 2018–2019 lava dome of Merapi volcano. *Bulletin of Volcanology*, *83*(2), 8. https://doi.org/10.1007/s00445-020-01428-x

Le Mével, H., Gregg, P. M., & Feigl, K. L. (2016). Magma injection into a long-lived reservoir to explain geodetically measured uplift: Application to the 2007–2014 unrest episode at Laguna del Maule volcanic field, Chile. *Journal of Geophysical Research: Solid Earth*, *121*(8), 6092–6108. https://doi.org/10.1002/2016JB013066

Lu, Y., Tan, Y., & Li, X. (2018). Stability analyses on slopes of clay-rock mixtures using discrete element method. *Engineering Geology*, *244*, 116–124. https://doi.org/10.1016/j.enggeo.2018.07.021

Luding, S. (2008). Introduction to discrete element methods: Basic of contact force models and how to perform the micro-macro transition to continuum theory. *European Journal of Environmental and Civil Engineering*, *12*(7–8), 785–826. https://doi.org/10.1080/19648189.2008.9693050

Marsden, L. H., Neuberg, J. W., Thomas, M. E., Mothes, P. A., & Ruiz, M. C. (2019). Combining Magma Flow and Deformation Modeling to Explain Observed Changes in Tilt. *Frontiers in Earth Science*, *7*. https://doi.org/10.3389/feart.2019.00219

Matsui, T., & San, K.-C. (1992). Finite Element Slope Stability Analysis by Shear Strength Reduction Technique. *Soils and Foundations*, *32*(1), 59–70. https://doi.org/10.3208/sandf1972.32.59

de' Michieli Vitturi, M., Clarke, A. B., Neri, A., & Voight, B. (2008). Effects of conduit geometry on magma ascent dynamics in dome-forming eruptions. *Earth and Planetary Science Letters*, *272*(3), 567–578. https://doi.org/10.1016/j.epsl.2008.05.025

Morand, A., Poppe, S., Harnett, C., Cornillon, A., Heap, M., & Mège, D. (2024). Fracturing and Dome-Shaped Surface Displacements Above Laccolith Intrusions: Insights From Discrete Element Method Modeling. *Journal of Geophysical Research: Solid Earth*, *129*(3), e2023JB027423. https://doi.org/10.1029/2023JB027423

Mreyen, A.-S., Donati, D., Elmo, D., Donze, F. V., & Havenith, H.-B. (2022). Dynamic numerical modelling of co-seismic landslides using the 3D distinct element method: Insights from the Balta rockslide (Romania). *Engineering Geology*, *307*, 106774. https://doi.org/10.1016/j.enggeo.2022.106774

Neuberg, J. W., Collinson, A. S. D., Mothes, P. A., C. Ruiz, M., & Aguaiza, S. (2018). Understanding cyclic seismicity and ground deformation patterns at volcanoes: Intriguing lessons from Tungurahua volcano, Ecuador. *Earth and Planetary Science Letters*, *482*, 193–200. https://doi.org/10.1016/j.epsl.2017.10.050

Nishimura, T. (2009). Ground deformation caused by magma ascent in an open conduit. *Journal of Volcanology and Geothermal Research*, *187*(3), 178–192. https://doi.org/10.1016/j.jvolgeores.2009.09.001

Norini, G., & Acocella, V. (2011). Analogue modeling of flank instability at Mount Etna: Understanding the driving factors. *Journal of Geophysical Research: Solid Earth*, *116*(B7). https://doi.org/10.1029/2011JB008216

Reid, M. E., Christian, S. B., & Brien, D. L. (2000). Gravitational stability of three-dimensional stratovolcano edifices. *Journal of Geophysical Research B: Solid Earth*, *105*(B3), 6043–6056. https://doi.org/10.1029/1999JB900310

Russo, G., Giberti, G., & Sartoris, G. (1997). Numerical modeling of surface deformation and mechanical stability of Vesuvius volcano, Italy. *Journal of Geophysical Research: Solid Earth*, *102*(B11), 24785–24800. https://doi.org/10.1029/97JB01776

Schaefer, L. N., Oommen, T., Corazzato, C., Tibaldi, A., Escobar-Wolf, R., & Rose, W. I. (2013). An integrated field-numerical approach to assess slope stability hazards at volcanoes: The example of Pacaya, Guatemala. *Bulletin of Volcanology*, *75*(6), 720. https://doi.org/10.1007/s00445-013-0720-7

Scholtès, L., & Donzé, F.-V. (2012). Modelling progressive failure in fractured rock masses using a 3D discrete element method. *International Journal of Rock Mechanics and Mining Sciences*, *52*, 18–30. https://doi.org/10.1016/j.ijrmms.2012.02.009

Scholtès, L., & Donzé, F.-V. (2013). A DEM model for soft and hard rocks: Role of grain interlocking on strength. *Journal of the Mechanics and Physics of Solids*, *61*(2), 352–369. https://doi.org/10.1016/j.jmps.2012.10.005

Scholtès, L., & Donzé, F. V. (2015). A DEM analysis of step-path failure in jointed rock slopes. *Comptes Rendus Mécanique*, *343*(2), 155–165. https://doi.org/10.1016/j.crme.2014.11.002

Siswowidjoyo, S., Suryo, I., & Yokoyama, I. (1995). Magma eruption rates of Merapi volcano, Central Java, Indonesia during one century (1890–1992). *Bulletin of Volcanology*, *57*(2), 111–116. https://doi.org/10.1007/BF00301401

Smilauer, V., Angelidakis, V., Catalano, E., Caulk, R., Chareyre, B., Chèvremont, W., et al. (2021). Yade documentation (Version 3rd). The Yade Project. https://doi.org/10.5281/zenodo.5705394

Tibaldi, A., Bistacchi, A., Pasquarè, F. A., & Vezzoli, L. (2006). Extensional tectonics and volcano lateral collapses: Insights from Ollagüe volcano (Chile-Bolivia) and analogue modelling. *Terra Nova*, *18*(4), 282–289. https://doi.org/10.1111/j.1365-3121.2006.00691.x

Vásárhelyi, B. (2009). A possible method for estimating the Poisson's rate values of the rock masses. *Acta Geodaetica et Geophysica Hungarica*, *44*(3), 313–322. https://doi.org/10.1556/AGeod.44.2009.3.4

Voight, B., & Elsworth, D. (1997). Failure of volcano slopes. *Géotechnique*, *47*(1), 1–31. https://doi.org/10.1680/geot.1997.47.1.1

Voight, Barry, Janda, R. J., & Glicken, H. (1983). Nature and mechanics of the mount St Helens rockslide — avalanche of 18 May 1980. *Geotechnique*, *20*(6), A176. https://doi.org/10.1016/0148-9062(83)90666-6

van Wyk de Vries, B., & Merle, O. (1998). Extension induced by volcanic loading in regional strike-slip zones. *Geology*, *26*(11), 983–986. https://doi.org/10.1130/0091-7613(1998)026<0983:EIBVLI>2.3.CO;2

References From the Supporting Information

Potyondy, D. O., & Cundall, P. A. (2004). A bonded-particle model for rock. *International Journal of Rock Mechanics and Mining Sciences*, *41*(8), 1329–1364. https://doi.org/10.1016/j.ijrmms.2004.09.011

Vinciguerra, S., Meredith, P. G., & Hazzard, J. (2004). Experimental and modeling study of fluid pressure-driven fractures in Darley Dale sandstone. *Geophysical Research Letters*, *31*(9). https://doi.org/10.1029/2004GL019638